Doubly resonant photonic antenna for single infrared quantum dot imaging at telecommunication wavelengths

Zhihua Xie,[†] Yannick Lefier,[†] Miguel Suarez,[†] Mathieu Mivelle,[†,‡] Roland Salut,[†] Jean-Marc Merolla,[†] and Thierry Grosjean[*,†]

Optics Department, FEMTO-ST Institute UMR 6174, Univ. Bourgogne Franche-Comté, CNRS

E-mail: thierry.grosjean@univ-fcomte.fr

Phone: +33 3 81 66 64 17. Fax: +33 3 81 66 67 01

Abstract

Colloidal Quantum dots (CQDs) have drawn a strong interest in the past years for their high perspectives in scientific, medical and industrial applications. However, the full characterization of these quantum emitters is currently restricted to the visible wavelengths and it remains a key challenge to optically probe single CQDs operating in the infrared spectral domain which is targeted by a growing number of applications. Here, we report the first experimental detection and imaging at room temperature of single infrared CQDs operating at telecommunication wavelengths. Imaging was done with a doubly resonant bowtie nano-aperture antenna (BNA) written at the end of a fiber nanoprobe, whose resonances spectrally fit the CQD absorption and emission wavelengths. Direct near-field characterization of PbS CQDs reveal individual

---

[*]To whom correspondence should be addressed

[†]FEMTO-ST

[‡]Current address: Université Pierre et Marie Curie, CNRS, Institut des NanoSciences de Paris, UMR 7588, 75005 Paris, France

nanocrystals with a spatial resolution of 75 nm ($\lambda/20$) together with their intrinsic 2D dipolar free-space emission properties and exciton dynamics (blinking phenomenon). Because the doubly resonant BNA is strongly transmissive at both the CQD absorption and emission wavelengths, we are able to perform all-fiber nano-imaging with a standard 20 % efficiency InGaAs avalanche photodiode (APD). Detection efficiency is predicted to be 3000 fold larger than with a conventional circular aperture tip of the same transmission area. Double resonance BNA fiber probes thus offer the possibility of exploring extreme light-matter interaction in low band gap CQDs with current plug-and-play detection techniques, opening up new avenues in the fields of infrared light emitting devices, photodetectors, telecommunications, bio-imaging and quantum information technology.

Introduction

Nanotechnologies rely on the ability to fabricate and manipulate nanosize structures, and to detect these nano-elements individually and characterize their intrinsic properties. The need for nanoscale detection and imaging is of crucial importance in the rapidly growing optoelectronic and biomedical technologies based on the engineering, manipulation and control of colloidal quantum dot (CQD).[1] In that domain, light emission is a direct means to locate CQDs and reveal their intrinsic nanoscale properties and dynamics. If the characterization of CQDs in the visible spectral range has been successfully achieved with optical imaging techniques directly derived from single molecule detection and spectroscopy, the characterization of CQDs in the infrared spectral domain remains extraordinary difficult, preventing a growing number of devices and applications targeting this wavelength range to reach their full potential.

Infrared CQDs are indeed among potential key building blocks in the engineering of modern infrared light sources, photodiodes and solar cells.[2–5] Owing to quantum size effect, infrared CQDs

2

have shown exceptional spectral tunability up to mid-infrared domain, thus leading to totally new paradigms in a wide field of applications ranging from telecommunications to biological imaging and photovoltaics.[6–9] Given their high photostability, infrared CQDs are also suitable candidates as single photon sources at room temperature for fiber compatible quantum information processing at telecommunication wavelengths.

Detecting and probing infrared CQDs at room temperature down to individual elements is highly desirable as it would allow for improved functionality and performance of these nanocrystals in the applications mentioned above. The modest spatial resolution of diffraction-limited far-field optics at infrared frequencies impedes the accurate imaging of single infrared CQDs at telecommunication wavelengths. Moreover, high numerical aperture (NA) objectives (NA>1) commonly used for single molecule detection are initially optimized for visible frequencies and are not corrected to operate in the infrared portion of the spectrum. Extending their operation to IR frequencies is possible but it involves implementing an ultra-low noise photon detector given the resulting drop of detection efficiency.[10,11] Higher detection efficiency is so far made at the expense of a detector operating at low temperature, which dramatically weighs down the acquisition system. The extension of this imaging technique, which is subject to chromatic dispersion, to the telecommunication spectral range (1460 nm<λ<1625 nm) is also questionable. To date, no study has reported the detection of single infrared nanocrystals at telecommunication wavelengths with far-field imaging approaches.

Scanning Near-field Optical microscopy (SNOM) provides alternative imaging systems free from bulky optics and capable of probing single fluorescent molecules and quantum dots with resolution well beyond the diffraction limit.[12,13] These plug-and-play nano-imaging architectures rely on a circular nano-aperture positioned at the end of a double taper fiber tip[14] which acts as a near-field interface between the nano-emitters and the optical fiber. Unfortunately, subwavelength circular nano-apertures operate beyond cutoff in their waveguide transmission process, which dramatically limits their optical throughput and collection efficiency, especially at near-infrared frequencies.[15]

3

The development of photonic nano-antennas has recently broken down the cutoff barrier in nanoscale optics, thus enabling unprecedented light enhancement and transmission down to the nanometer scale in a spectral domain spanning from visible to infrared regime (and beyond).[16] Aperture nano-antennas, such as bowtie nano-aperture antenna (BNA),[17,18] have been successfully integrated at the apex of fiber tips for nano-imaging applications.[19] Their nanoscale resonant transmission properties below cutoff led to background-free ultra-bright light sources for single molecule imaging at visible frequencies[20] and highly sensitive light nano-collectors for photonic crystal near-field mapping at the infrared telecommunication window.[21] In these applications, the nano-antenna single resonance is tuned to the portion of the spectrum related to the study.

In this paper, we propose a new type of nano-antenna fiber probe based on a doubly resonant BNA for imaging single infrared CQDs at telecommunication wavelengths. Our design relies on a BNA showing two spectrally separated resonances tuned to the nanocrystal's absorption and emission wavelengths (visible and telecommunication spectra, respectively), thus providing an efficient two-way communication channel between single CQDs and the optical fiber for both nanocrystal optical excitation and fluorescence collection. The first resonance at visible wavelengths allows for enhancing the emitter excitation rate whereas the second resonance at near-infrared frequencies ensures a nanoscale collection process right below cutoff, i.e., the best compromise between collection efficiency and aperture size. This new approach is demonstrated with the first imaging of single PbS CQDs at telecommunication wavelengths (λ=1500 nm). The sensitivity of the resulting fiber probe is large enough to detect single CQDs with a conventional 20% efficiency InGaAs photon counter. The resulting all-fiber optical bench is then ultracompact (free from bulky optics) and yields $\lambda/20$ spatial resolution (i.e., 75 nm). Beyond the imaging of the spatial distribution of single PbS CQDs on a surface, the new BNA nanoprobe reveals PbS nanocrystal's 2D dipolar emission properties and intrinsic blinking phenomenon. These results are highly relevant in the context of the growing interest in understanding and controlling fundamental properties of semiconductor nano-crystals dedicated to the infrared regime and more especially to telecommunication wavelengths.

Results and discussion

In order to produce the doubly resonant BNA fiber probe, polymer tips are first grown by pho-topolymerization at the cleaved end facet of a single mode fiber (SMF-28).[22] The tips are about 40 μm long and have radius of curvature of 500 nm at their apex. Next, the probes are metal coated with a few nanometers thick titanium adhesion layer followed by a silver layer that is 200-350 nm thick. Silver is chosen for its high conductivity and minimum losses ensuring strong antenna effect. The tip apex is then polished by Focused Ion Beam (FIB) milling to reduce metal layer thickness on top to 200 nm (for each production batch, one sacrificial metal-coated tip is cut by FIB in order to estimate metal thickness at the tip apex and thus calibrate the polishing process). As noted below, at such a metal layer thickness, one of the two resonances of the BNA is spectrally centered on the absorption wavelength of the inspected CQDs. Finally, a 280 nm wide BNA with a square gap of 40 nm is opened at the tip apex by FIB milling. 1(a) and (b) display SEM micrographs of a resulting all-fiber nano-imaging platform. Given the fast decay of silver under ambient conditions, tip metal coating was immediately followed by BNA writing. Then, the tips were kept in a clean and dry environment before near-field imaging which was done during the next few days following metal coating.

The optical response of this new nano-antenna probe is simulated using three dimensional Finite Difference in Time Domain method (3D FDTD) available from a commercial software pro-gramme (Fullwave, Synopsis). 2(a) shows the emission spectrum of a BNA probe placed 15 nm above a 20 nm thick PMMA layer onto a semi-infinite medium of SiO_2 (see Methods). In the simulation, the BNA is excited with a gaussian beam launched within the tip at a distance of 4.5 μm from the BNA. The incident waves are temporally described by a single pulse and are linearly polarized along the BNA's symmetry axis that crosses its two metal triangles (parallel to (0x)). The time-varying electric field component E_x transmitted by the nano-antenna is recorded at a single cell aligned with the tip symmetry axis and located 20 nm away from the BNA, within the PMMA layer (ie, 5 nm below the free interface of the PMMA layer). The spectrum of $|E_x|^2$ is calculated by Fourier-transforming this result.
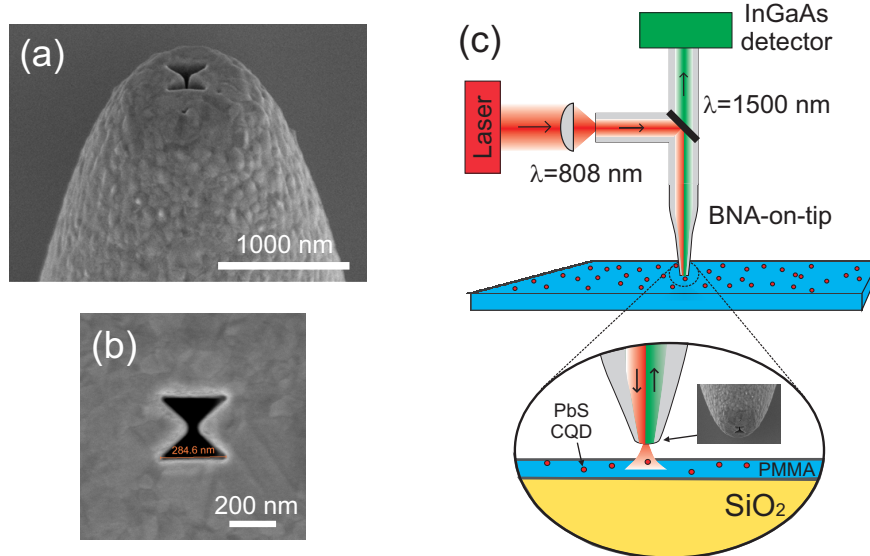
Figure 1: (a,b) SEM micrographs of a doubly resonant BNA on a fiber tip: (a) side view of the tip apex and (b) top view of the BNA. (c) Schematic diagram of the experimental configuration: in-fiber excitation of the BNA is performed at λ=808 nm with light linearly polarized along the polarization axis of the BNA. The tip is set 15 nm above the surface of a 20 nm thick PMMA layer containing single PbS quantum dots and it is raster scanned across the sample. During scanning, fluorescence signal at wavelengths around 1550 nm is collected by the BNA and detected through the fiber with a standard InGaAS APD.

The nanoprobe shows two resonances at wavelengths around 800 nm and 1550 nm. To understand the origin of this double resonance, one may consider the BNA as a nano-structure which confines light on the basis of the excitation of a highly confined guided mode bound to its nanometer size gap.[23,24] A BNA of finite length, limited by the thickness of the metal layer, imposes boundary conditions on this guided mode and leads to Fabry-Perot resonances, which is a unique property of metallic nano-apertures operating below cutoff.[25,26] The first resonance (at λ =1550 nm), noted FP0, appears right at the cutoff of the nanoscale waveguide (it has near-zero effective refractive index) and thus does not undergo spectral dependence on BNA length. The second resonance (at 808 nm), noted FP1, is the first Fabry-Perot harmonic of finite phase velocity which can be spectrally tuned with the structure length. Such a response discrepancy between FP0 and FP1 with respect to antenna geometrical parameters allows for spectrally tuning the two BNA resonances independently from each other: FP0 spectral response is mainly governed by the BNA lateral size and gap width whereas FP1 is controlled by varying metal layer thickness (ie. aperture

6

length).[23,24] Both FP0[19,21] and FP1[20] resonances of a BNA are at the origin of important field enhancements within the structure and have demonstrated remarkable performances for near-field microscopy, in terms of resolution and throughput. However, they have never been combined yet for optical applications. Note that the remarkable properties of the FP0 mode in the extraordinary optical transmission reported so far[21,27,28] have been obtained for multi-photon excitations.
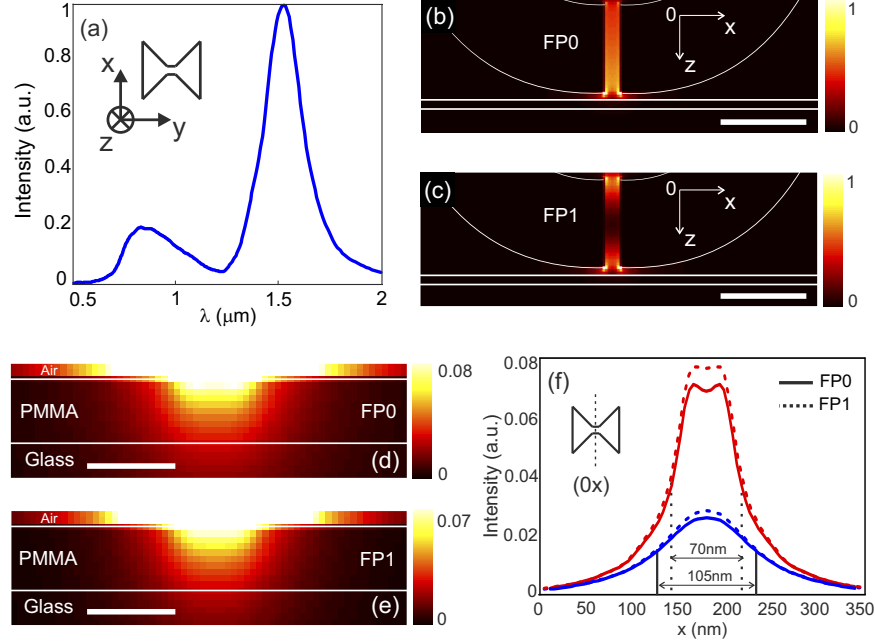

Figure 2: (a) Theoretical resonance spectrum of a doubly resonant BNA on a tip, positioned at a distance of 15 nm above the surface of a 20 nm thick PMMA layer lying on a semi-infinite glass substrate. The excitation wave is launched into the tip body and is linearly polarized along the polarization axis (0x) of the BNA (ie. the symmetry axis of the BNA that crosses the two metal triangle). (b-f) Simulation of the optical electric intensity produced by (b,d) FP0 resonance at $\lambda = 1500$ nm and (c,e) FP1 resonance at $\lambda = 808$ nm in the longitudinal plane (0xz) that contains the BNA's polarization axis (see inset of (a)): (b,c) large scale views of the tip apex (scalebar: 200 nm) and (d,e) intensity plots right at the 20 nm thick PMMA layer (scalebar: 70 nm). (f) Cross sections along the (0x)-axis (see inset) of the light spots shown in (d) (solid lines) and (e) (dashed lines), at the upper (red curves) and lower (blue curves) interfaces of the thin PMMA layer.

2(b-e) show simulations of electric intensity distributions produced by the BNA on a tip, at the CQD's emission and absorption wavelengths, (b,d) 1500 nm and (c,e) 808 nm, respectively. The tip model is the same as the one used for spectrum calculations (see Method) except that a continuous waves is launched into the tip at the two wavelengths of interest (one simulation per wavelength). Intensity plots are simulated along the longitudinal (0xz)-plane, for an excitation

7

polarization parallel to the BNA's polarization axis (0x). We see from 2(b) and (c) that the two FP0 and FP1 modes are strongly bound to the BNA nanometer-scale feed gap: FP0 shows an almost uniform intensity distribution along the gap which evidences near-zero effective refractive index of the mode, whereas FP1 is described by a single intensity node at half the BNA length. Both resonances allow for dramatically confining optical fields within the PMMA layer, as shown in 2(d) and (e). The spot size within PMMA layer varies from 70 nm (better than $\lambda/20$) right underneath its top free surface up to 105 nm (around $\lambda/15$) at the bottom PMMA/glass interface (see 2(f)).

To evaluate the role and performances of the FP0 and FP1 resonances in the imaging of single infrared CQD, we numerically simulated, with FDTD, three different BNA geometries and a circular aperture opened on the same kind of tip and in near-field interaction with a single QE. Following a classical approach of the coupling between a QE and a nano-antenna, where the QE is modeled with a radiating dipole,[29,30] the emitter excitation rate γ_{exc} and the collection yield of the aperture tip q_{tip} can be defined as:

$$\gamma_{exc} = \mathbf{n} \cdot |\mathbf{E}_{exc}(\mathbf{r})|^2, \tag{1}$$

$$q_{tip} = \frac{\gamma_{tip}}{\gamma_{tot}} = \frac{P_{tip}}{P_{tot}}. \tag{2}$$

where $\mathbf{n}$ is the unit vector along the absorption dipole moment of the QE. $\mathbf{E}_{exc}(\mathbf{r})$ is the complex electric field vector emanating from the different apertures at the dipole's position $\mathbf{r}$ and at the excitation wavelength ($\lambda = 808$ nm). q_{tip} is obtained by inserting a dipole source at the desired QE's position, radiating a continuous wave at QE's emission wavelength ($\lambda = 1500$ nm). It is calculated as the power P_{tip} transmitted into the tip (via Poynting vector flux calculation) normalized by the total power P_{tot} dissipated by the dipole source.[29,30] It corresponds to the ratio between the radiative decay rate of the emitter within the tip (γ_{tip}) to its total decay rate (γ_{tot}). Tip and sample models remain unchanged (see Methods). The four aperture tips are considered to probe a single quantum emitter of absorption and emission dipole moments oriented along (0x) and positioned

along the tip symmetry axis, 5 nm underneath the free surface of the PMMA layer. The geometrical description of the three BNA apertures, defined by the parameters width/gap-size/length, are set to 280 nm/40 nm/200 nm for the first BNA (BNA_1, cf. 1), 250 nm/40 nm/70 nm for the second BNA (BNA_2) and 440 nm/40 nm/170 nm for the third BNA (BNA_3), respectively. The circular aperture has a diameter of 226 nm to match its transmission area to BNA_1's. It is opened at the end of the same tip covered by a 200-nm thick silver layer.
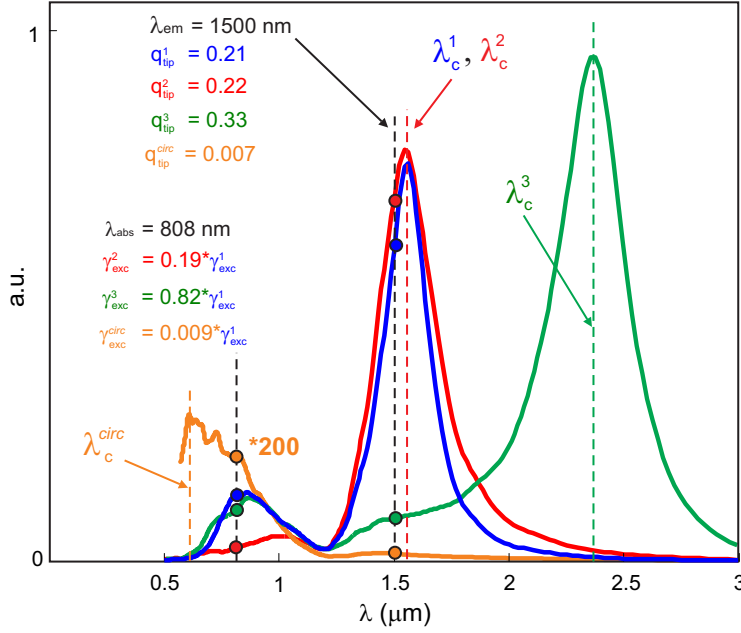

Figure 3: Theoretical resonance spectra of three different BNAs (BNA_i, $i = 1, 2, 3$) and one circular aperture opened at the end of silver-coated tips, together with their excitation rates at λ=808 nm (γ_{exc}^i, $i = 1, 2, 3$ for the three BNAs and γ_{exc}^{circ} for the circular aperture) and tip collection yields at λ=1500 nm (q_{tip}^i, $i = 1, 2, 3$ for the three BNAs and q_{tip}^{circ} for the circular aperture). λ_c^i ($i = 1, 2, 3$) and λ_c^{circ} are the cutoff wavelengths of the three BNAs and the circular aperture, respectively, above which the transmission through the apertures strongly decreases. The tips are positioned 15 nm above the surface of a 20 nm thick PMMA layer lying on a semi-infinite glass substrate. Blue curve: resonance of BNA_1, red curve: resonance of BNA_2, green curve: resonance of BNA_3, orange curve: resonance of the circular aperture.

3 shows the transmission spectra of these four apertures (calculation is detailed above) together with their excitation rate and collection yield. Both BNA_1 and BNA_2 have a FP0 resonance centered on λ=1.55 μm (cf. 2 for BNA_1), i.e., their cutoff wavelengths λ_1^c and λ_2^c, respectively, are slightly red-shifted with respect to the QE's emission wavelength. The cutoff wavelength λ_3^c of BNA_3 is

noticeably red-shifted with respect to the QE's emission wavelength (FP0 centered **on** $\lambda = 2.4 \mu \mathbf{m}$) whereas the cutoff wavelength λ_{circ}^{c} of the circular aperture is blue-shifted below the absorption wavelength of the QE.

The collection efficiencies of BNA_1 and BNA_2, right below cutoff are almost equal to 21%, whereas the tip collection efficiency of BNA_3, which operates well below cutoff reaches 33%. In the context of the collection of single photons, the FP0 resonance offers a straightforward means to spectrally locate the aperture cutoff, which can thus be easily tuned at will up to telecommunication wavelengths (and beyond), while keeping a nanometer confinement and resolution ability to the SNOM aperture tip. Below cutoff, the aperture provides an efficient nanoscale channel in-between the QE and the tip, whereas beyond cutoff the two-way transmission channel is almost closed and the collected signal drops, as observed with the circular aperture whose collection efficiency is equal to 0.7%. By tuning FP0 to the CQD emission wavelength, we directly find the best compromise between collection efficiency and nano-antenna size, which is a critical parameter in the frame of the accurate engineering of ultra-small apertures at the apex of a sharp tapered tip. 3 also shows that the role of FP1 is to enhance the emitter excitation rate γ_{exc}. BNA_2, which shows a single resonance at λ=1.55 μm (no FP1 resonance at 808 nm), provides an excitation rate 5.3 fold smaller than BNA_1 whose resonance FP1 increases the excitation optical field at the emitter's absorption wavelength. The role of FP1 is critical in the nano-imaging of CQDs with a SNOM tip as it allows the limiting of the incident power into the tip, thus reducing tip heating. From this analysis, we predict that the fluorescence signal collected by an aperture tip, defined as $\eta = \gamma_{exc} q_{tip}$, is more than 3000 times larger with the doubly resonant BNA_1 than with a 226 nm wide circular aperture of identical transmission area. Moreover, the resolution ability of the resulting circular aperture is comparatively modest, emphasizing the potential of our doubly resonant BNA to probe single infrared CQDs.

To demonstrate experimentally the doubly resonant BNA for single infrared CQD imaging, we probed single PbS quantum dots (from Evident) whose luminescence center wavelength is about 1500 nm. The choice of PbS CQDs is motivated by their high potentialities in photovoltaics and

photodetectors[31,32] as well as in the realization of tunable light sources, amplifiers and modulators at telecommunication wavelengths.[33–36]

The imaging set-up is shown in 1(c). PbS CQDs are randomly embedded in a 20 nm thick PMMA layer deposited onto a microscope coverslip (see Methods). Manufacturer ensures CQDs of 5.3 nm large crystalline core and 9.3 nm overall size (core and shell). There should however be a little size dispersion within the sample. The doubly resonant BNA nanoprobe is mounted in a commercial SNOM (NTegra, from NT-MDT company) to be raster scanned across single CQDs at a nanometer distance from the sample surface. Tip-to-sample distance is kept constant (within 15 nm) with a shear-force feedback loop. Note that the spectral position of resonances are dependent on the distance between the tip and the surface, especially at the considered short tip-to-sample spacings.[37] Because the tip-to-sample distance is known with an accuracy of ± 5nm, the resulting uncertainty in the resonance spectral positions is predicted to not exceed $\pm$ 15 nm,[37] which has a negligible consequence on the signal detection in our case. Single CQDs are locally excited by the nano-antenna with in-fiber illumination at λ=808 nm from a laser diode (BlueSky Research). The impinging laser light is spectrally filtered before reaching the nano-antenna to avoid the detection of an undesired parasitic background signal at the nanocrystal's emission wavelengths. About 50 μW are injected into the fiber piece whose output end facet is grafted with the BNA on a tip. Since the fiber (SMF-28) is multimode at λ=808 nm, a few loops are performed onto the fiber to filter out its undesired high-order guided modes and ensure tip excitation with a confined fundamental mode. The resulting mode leakage induces the loss of a part of the input power. The polarization state of the excitation photons is defined with a fiber polarization controller. Spontaneous emission is collected by the same nano-antenna and transferred backward through the same fiber to an add-drop filter which extracts and transfers fluorescence photons within the bandwidth 1500 nm-1620 nm towards 20 % efficiency InGaAs photon counter (LYNXEA-M1 from AUREA Technology company). The detector is directly connected to the SNOM control unit for image acquisition.

The fluorescence image reported in 4(a) is 1.8 μm wide and is acquired at a scan speed of 2.34μm/s. We see a series of single circular spots of various brightness and almost constant size.

4(b) displays a close range scan of one of the single quantum dots of 4(a). A Gaussian fit of the experimental cross section reveals a full width at half maximum at a single spot of 75 nm ($\lambda/20$) which is in correct agreement with the spot size values predicted for both resonances of the BNA (2(f)). The signal-to-noise level, larger than 3, is high enough to localize the nanoscrystals onto the surface and analyze their spatial distribution and emission properties. 4(c) and (d) show the time trace acquired when the nano-antenna probe is positioned directly on a single quantum dot at two different input powers 50 μW and 250 μW into the fiber (two different tips were used). Two-state blinking is observed, confirming single quantum dot distribution within the PMMA layer. The blinking phenomenon remains weak and photon emission is turned off during short time delays at the lower input power (4(c)) and becomes stronger, with longer off-state durations, at the higher input power (4(d)), which is in agreement with colloidal quantum dot emission properties.[38] Note that the detector integration time chosen here reveals emission intermittency over periods larger than one second. According to the simulation of the light confinements produced by the doubly resonant BNA within the PMMA layer (2(f)), the bright spots of FWHM equal to 78,1 $\pm$ 4.6 nm observed in 4(a) show that mainly the upper CQDs can be seen due to the higher near-field intensity.

Given the dipolar properties of BNAs,[20,21,39] 4(a) also provides information regarding the orientation properties of the transition dipole moment of single PbS CQDs. The distribution of near constant isotropic circular single-spot patterns observed within 4(a) do not match the near-field images of single fluorescent molecules which show a variety of different patterns under BNA imaging, depending on the orientation of the molecule's absorption dipole moment.[20] This confirms that the PbS CQD fluorescence process is not driven by a 1D oriented dipole moment but rather by a 2D dipole moment parallel to the sample surface, as is the case for visible colloidal quantum dots.[40,41] They do not undergo a fixed transition dipole moment in the sample plane (i.e., they are not selective with respect to incident polarization), as for single molecules, and uniform isotropic optical patterns are detected at nanocrystal positions despite the highly anisotropic BNA's optical response.[20,21] This means that the orientation of the absorption and emission dipole moments
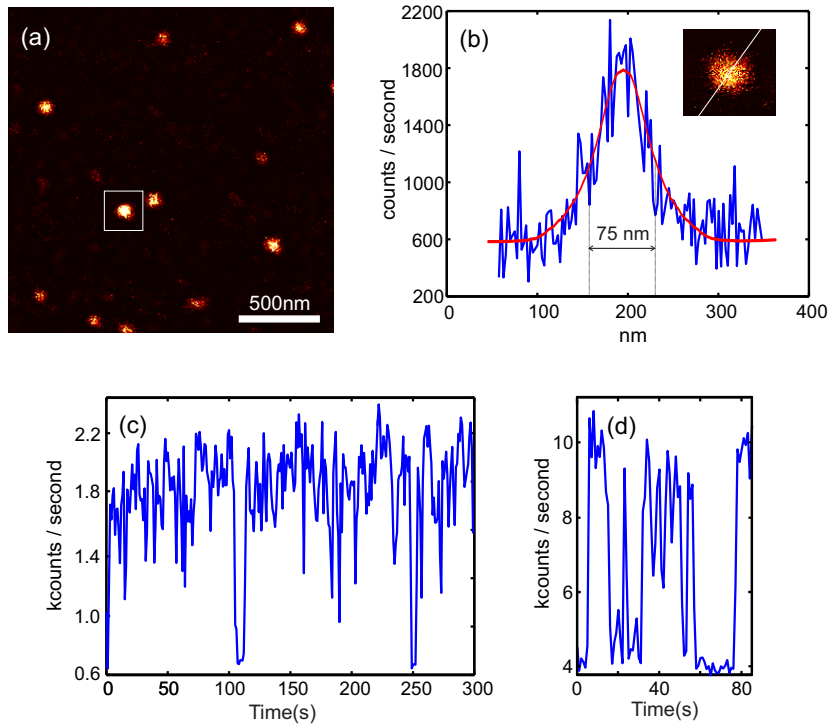
Figure 4: The doubly resonant BNA on fiber tip reveals single near-infrared PbS CQDs as single tiny circular spots. (a) Image of the quantum dots with the all-fiber platform: the in-fiber excitation waves are polarized along the BNA polarization axis and the signal is collected through the same nanostructure. (b) Intensity profile of a single quantum dot shown in the figure inset (along the white line of the inset): the quantum dot is located in the rectangle of (a). (c) Time trace acquired when the doubly resonant BNA is located right at a single nanocrystal with an input power into the fiber of 50 μW, revealing blinking phenomenon.(d) Time trace at a single nanocrystal with an input power into the fiber of 250 μW (integration time: 1 second).

13

are controlled by the two dipolar resonances of the BNA, respectively, leading to nearly constant single spot shapes within the acquisition area. The different intensities measured throughout the single spot distribution may then reveal slight anisotropies in the 2D dipole moments of the CDQs (leading to more or less overlap with the BNA's dipole emission and collection) and/or quantum dots of non-uniform absorption cross-sections and/or intrinsic quantum yields.

The dipolar properties of the BNA, which are common to all gap-based nano-antennas, associate the generation of a tiny "hot spot" to a high sensitivity of the nanostructure to the excitation polarization:[39] the tight optical confinement generated at antenna gap for polarization parallel to its polarization axis is canceled and the maximum intensity over the antenna is strongly reduced if the polarization direction is rotated by $90°$. As a result, the excitation rate is enhanced over a tiny area within the emitter plane for polarization parallel to the BNA's polarization axis (5(a)) and it is less confined and reduced by a factor of 16.7 for the perpendicular polarization (5(c)). 5(b) and (d) show the single PbS CQD response for excitation polarization parallel and perpendicular to the BNA's polarization axis, respectively. When the BNA is resonantly excited, the image shows well-defined spots beyond noise level. When the polarization direction is turned by $90°$, the single quantum dot patterns are much closer to the noise level, the detected signal being 3.6 times smaller. The level of the detected signals observed in 5(b) and 5(d) reflects the polarization properties of the BNA (shown in 5(a) and (c)), the CQD imaging process thus relies on the BNA itself. The decrease of the detected signal observed experimentally, smaller than the theoretically predicted reduction of excitation rate, can be partly explained by the difficulty to accurately define the two desired orthogonal polarizations of the incident waves (parallel and perpendicular to the BNA's main axis) in a few-mode fiber with a far-field monitoring through the BNA (ie., a tiny linear polarizer).

Conclusion

In conclusion, we demonstrated the unprecedented ability of photonic antennas to bridge the gap between optical imaging and infrared CQD analysis at telecommunication wavelengths which re-
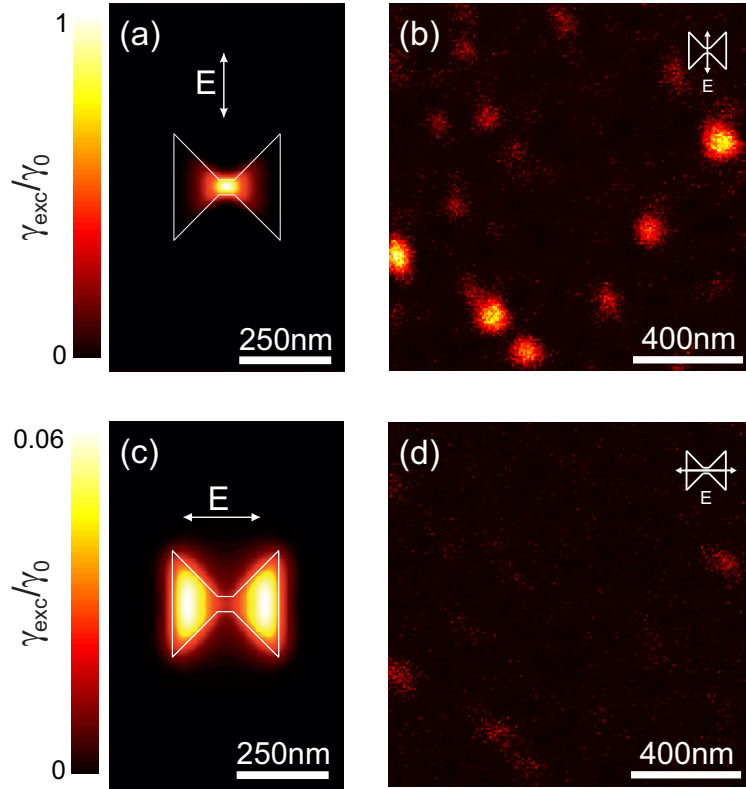
Figure 5: The BNA is demonstrated in the local imaging of single PbS CQDs. (a,c) Simulation of the distribution of normalized excitation rate produced by the FP1 resonance of the BNA at λ=808 nm plotted in the transverse plane taken 5 nm underneath the free surface of the PMMA layer, for (a) and (c) the two excitation polarization directions parallel and perpendicular to the BNA's polarization axis (see arrows), respectively. γ_0 is the maximum excitation rate calculated for the incident polarization parallel to the BNA's polarization axis. (b,d) Images of PbS quantum dots acquired for excitation polarization parallel and perpendicular to the BNA's polarization axis (see insets), respectively. These two images refer to the normalized excitation rates shown in (a) and (c), respectively.

mains relatively unexplored optically despite highly promising perspectives. We introduced the concept of doubly resonant BNA on a fiber tip as an ultracompact near-field optical probe enabling PbS CQD detection and imaging at a wavelength of 1.5 μm with a standard 20% efficiency InGaAs photon counter. The method is totally new and paves the way towards full optical characterization schemes of infrared CQDs down to single elements, leading to potential improvements in the development of devices and methods within the telecommunication spectral range. Our nanoprobe has great potential in the study, quantification and optimization of the antibunching effect from infrared CQDs capable of providing room temperature single photon sources at telecommunication wavelengths. Our all-fiber nano-antenna platform also holds high promises in harnessing these size tunable on-demand single photon sources to optical fiber networks for the development of ultracompact fibered architectures for quantum information processing at telecommunication wavelengths.

Methods

The model used for all calculations of our nanoprobe consists of a volume spanning ± 3 μm in (0x) and (0y) about the apex of the fiber tip. The apex, with a tip-radius of 500 nm, is located at x=y=z=0 and the simulation spans 1.5 μm below the tip in air, and terminates 5 μm into the body of the tip. The tip geometry considered in this study is that of a polymer tip of refractive index equal to 1.52 and taper angle of 16°. Silver and PMMA are considered dispersive. The dispersion of silver is described by a Drude Lorentz model. The index of the glass substrate is set to 1.5. All six boundaries of the computation volume are terminated with perfectly matched layers in order to avoid parasitic unphysical reflections around the probe. The non-uniform grid resolution varies from 25 nm for portions at the periphery of the simulation, to 5 nm within the volume of the BNA and at the region immediately around the structure. Along (0z) axis, gridding is set down to 2 nm within the PMMA layer and 1.5 nm at the air gap between the tip and the sample.

Preparation of QD samples. We used PbS quantum dots from Evident Company diluted at a

concentration of 22.7 nmol/mL. 1.5 μL of original solution is diluted in 85 μL toluene and 15μL PMMA (4% PMMA in anisole). The mixture is kept for 30 minutes in an ultrasound bath to cancel QD aggregates. The solution is then spin coated onto a microscope coverslip at a speed of 2000 rps. Prior to spin coating, the microscope coverslip is cleaned in a mixture of alcohol and acetone (held for 10 minutes in an ultrasound bath) and dried by N_2 gas blowing. After spin coating, the QDs are randomly distributed within a 20 nm thick PMMA layer (layer thickness has been measured by Atomic Force Microscopy).

Acknowledgement

References

(1) Alivisatos, A. P. *Science* **1996**, *271*, 933.

(2) Rogach, A. L.; Eychmüller, A.; Hickey, S. G.; Kershaw, S. V. *Small* **2007**, *3*, 536–557.

(3) H Sargent, E. *Adv. Mater.* **2005**, *17*, 515–522.

(4) Kershaw, S. V.; Harrison, M.; Rogach, A. L.; Kornowski, A. *IEEE J. Sel. Top. Quant.* **2000**, *6*, 534–543.

(5) Keuleyan, S.; Lhuillier, E.; Brajuskovic, V.; Guyot-Sionnest, P. *Nat. Photonics* **2011**, *5*, 489–493.

(6) Tang, J.; Sargent, E. H. *Adv. Mater.* **2011**, *23*, 12–29.

(7) Harrison, M.; Kershaw, S.; Burt, M.; Rogach, A.; Kornowski, A.; Eychmüller, A.; Weller, H. *Pure Appl. Chem.* **2000**, *72*, 295–307.

(8) Medintz, I. L.; Uyeda, H. T.; Goldman, E. R.; Mattoussi, H. *Nat. Mater.* **2005**, *4*, 435–446.

(9) Kim, S.; Lim, Y. T.; Soltesz, E. G.; De Grand, A. M.; Lee, J.; Nakayama, A.; Parker, J. A.; Mihaljevic, T.; Laurence, R. G.; Dor, D. M.; Cohn, L. H.; Bawendi, M. G.; Frangioni, J. V. *Nat. Biotechnol.* **2004**, *22*, 93–97.

(10) Correa, R. E.; Dauler, E. A.; Nair, G.; Pan, S. H.; Rosenberg, D.; Kerman, A. J.; Molnar, R. J.; Hu, X.; Marsili, F.; Anant, V.; Berggren, K. K.; Bawendi, M. G. *Nano Lett.* **2012**, *12*, 2953–2958.

(11) Bischof, T. S.; Correa, R. E.; Rosenberg, D.; Dauler, E. A.; Bawendi, M. G. *Nano letters* **2014**, *14*, 6787–6791.

(12) Hosaka, N.; Saiki, T. *J. Microsc.* **2001**, *202*, 362–364.

(13) Matsuda, K.; Saiki, T.; Nomura, S.; Mihara, M.; Aoyagi, Y.; Nair, S.; Takagahara, T. *Phys. Rev. Lett.* **2003**, *91*, 177401.

(14) Saiki, T.; Mononobe, S.; Ohtsu, M.; Saito, N.; Kusano, J. *Appl. Phys. Lett.* **1996**, *68*, 2612–2614.

(15) Tsumori, N.; Takahashi, M.; Sakuma, Y.; Saiki, T. *Appl. Opt.* **2011**, *50*, 5710–5713.

(16) Novotny, L.; van Hulst, N. *Nat. Photonics* **2011**, *5*, 83–90.

(17) Wang, L.; Uppuluri, S.; Jin, E.; Xu, X. *Nano Lett.* **2006**, *6*, 361.

(18) Jensen, R. A.; Huang, I.-C.; Chen, O.; Choy, J. T.; Bischof, T. S.; Loncar, M.; Bawendi, M. G. *ACS Photonics* **2016**, *3*, 423–427.

(19) Mivelle, M.; Ibrahim, I. A.; Baida, F.; Burr, G. W.; Nedeljkovic, D.; Charraut, D.; Rauch, J.-Y.; Salut, R.; Grosjean, T. *Opt. Express* **2010**, *18*, 15964–15974.

(20) Mivelle, M.; van Zanten, T. S.; Neumann, L.; van Hulst, N. F.; Garcia-Parajo, M. F. *Nano Lett.* **2012**, *12*, 5972–5978.

(21) Vo, T.-P.; Mivelle, M.; Callard, S.; Rahmani, A.; Baida, F.; Charraut, D.; Belarouci, A.; Nedeljkovic, D.; Seassal, C.; Burr, G.; Grosjean, T. *Opt. Express* **2012**, *20*, 4124–4135.

(22) Bachelot, R.; Ecoffet, C.; Deloeil, D.; Royer, P.; Lougnot, D.-J. *Appl. Opt.* **2001**, *40*, 5860–5871.

(23) Guo, H.; Meyrath, T. P.; Zentgraf, T.; Liu, N.; Fu, L.; Schweizer, H.; Giessen, H. *Opt. Express* **2008**, *16*, 7756–7766.

(24) Ibrahim, I. A.; Mivelle, M.; Grosjean, T.; Allegre, J.-T.; Burr, G.; Baida, F. *Opt. Lett.* **2010**, *35*, 2448–2450.

(25) Cao, Q.; Lalanne, P. *Phys. Rev. Lett.* **2002**, *88*, 057403.

(26) Liu, H.; Lalanne, P. *Nature* **2008**, *452*, 728–731.

(27) Kinzel, E. C.; Xu, X. *Opt. Lett.* **2010**, *35*, 992–994.

(28) Barakat, E.; Bernal, M.-P.; Baida, F. *Opt. Express* **2010**, *18*, 6530–6536.

(29) Novotny, L.; Hecht, B. *Principle of nano-optics*; Cambridge University Press, 2006.

(30) Kaminski, F.; Sandoghdar, V.; Agio, M. *J. Comput. Theor. Nanosci.* **2007**, *4*, 635–643.

(31) McDonald, S. A.; Konstantatos, G.; Zhang, S.; Cyr, P. W.; Klem, E. J.; Levina, L.; Sargent, E. H. *Nat. Mater.* **2005**, *4*, 138–142.

(32) Zhao, N.; Osedach, T. P.; Chang, L.-Y.; Geyer, S. M.; Wanger, D.; Binda, M. T.; Arango, A. C.; Bawendi, M. G.; Bulovic, V. *ACS Nano* **2010**, *4*, 3743–3752.

(33) Bakueva, L.; Musikhin, S.; Hines, M.; Chang, T.-W.; Tzolov, M.; Scholes, G.; Sargent, E. *Appl. Phys. Lett.* **2003**, *82*, 2895–2897.

(34) Steckel, J. S.; Coe-Sullivan, S.; Bulović, V.; Bawendi, M. G. *Adv. Mater.* **2003**, *15*, 1862–1866.

(35) Grandidier, J.; Des Francs, G. C.; Massenot, S.; Bouhelier, A.; Markey, L.; Weeber, J.-C.; Finot, C.; Dereux, A. *Nano Lett.* **2009**, *9*, 2935–2939.

(36) Klem, E. J.; Levina, L.; Sargent, E. H. *Appl. Phys. Lett.* **2005**, *87*, 053101.

(37) Atie, E. M.; Tannous, T.; Grosjean, T.; Baida, F. I. *Applied Physics B* **2015**, *120*, 581–586.

(38) Banin, U.; Bruchez, M.; Alivisatos, A.; Ha, T.; Weiss, S.; Chemla, D. *J. Chem. Phys.* **1999**, *110*, 1195–1201.

(39) Jin, E. X.; Xu, X. *Appl. Phys. Lett.* **2005**, *86*, 111106–111106.

(40) Chung, I.; Shimizu, K. T.; Bawendi, M. G. *Proc. Natl. Acad. Sci.* **2003**, *100*, 405–408.

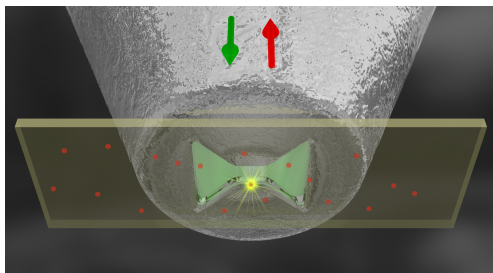(41) Empedocles, S. A.; Neuhauser, R.; Bawendi, M. G. *Nature* **1999**, *399*, 126–130.

Figure 6: For TOC only